Frontiers in Bioscience Landmark

Front. Biosci. (Landmark Ed) **2023**; 28(1): 19
https://doi.org/10.31083/j.fbl2801019

Original Research

Hybrid Nanoparticles of Manganese Oxide and Highly Reduced Graphene Oxide for Photodynamic Therapy

Haseeb A. Khan[1,*], Yong-kyu Lee[2], Mohammed Rafi Shaik[3], Nikhat J. Siddiqi[1], Mohamed R. Siddiqui[3], Sara T. Alrashood[4], Amal S. Alharbi[4], Aishah A. Ekhzaimy[5]

[1]Department of Biochemistry, College of Science, King Saud University, 11451 Riyadh, Saudi Arabia
[2]Department of Chemical and Biological Engineering, Korea National University of Transportation, 27469 Chungju, Republic of Korea
[3]Department of Chemistry, College of Science, King Saud University, 11451 Riyadh, Saudi Arabia
[4]Department of Pharmaceutical Chemistry, College of Pharmacy, King Saud University, 11451 Riyadh, Saudi Arabia
[5]Division of Endocrinology, Department of Medicine, King Saud University Medical City, 12372 Riyadh, Saudi Arabia
*Correspondence: khan_haseeb@yahoo.com; haseeb@ksu.edu.sa (Haseeb A. Khan)
Academic Editor: Peter Brenneisen
Submitted: 15 October 2022 Revised: 13 December 2022 Accepted: 15 December 2022 Published: 18 January 2023

Abstract

Background: Graphene-based nanomaterials possess unique optical, physicochemical and biomedical properties which make them potential tools for imaging and therapy. Manganese oxide nanoparticles are attractive candidates for contrast agents in magnetic resonance imagint (MRI). We used manganese oxide (Mn_3O_4) and highly reduced graphene oxide (HRG) to synthesize hybrid nanoparticles (HRG-Mn_3O_4) and tested their efficacy for photodynamic therapy (PDT) in breast cancer cells. **Methods**: The newly synthesized nanoparticles were characterized by transmission electron microscopy (TEM), energy-dispersive X-ray (EDX) spectroscopy, UV-visible spectroscopy, Fourier-transform infrared (FT-IR) spectroscopy, thermogravimetry, and X-ray diffraction (XRD) analyses. We used standard protocols of cytotoxicity and PDT after exposing A549 cells to various concentrations of hybrid nanoparticles (HRG-Mn_3O_4). We also performed fluorescence microscopy for live/dead cellular analysis. A549 cells were incubated with nanoparticles for 24 h and stained with fluorescein diacetate (green emission for live cells) and propidium iodide (red emission for dead cells) to visualize live and dead cells, respectively. **Results**: The cell viability analysis showed that more than 98% of A549 cells survived even after the exposure of a high concentration (100 μg/mL) of nanomaterials. These results confirmed that the HRG-Mn_3O_4 nanoparticles are nontoxic and biocompatible at physiological conditions. When the cell viability analysis was performed after laser irradiation, we observed significant and concentration-dependent cytotoxicity of HRG-Mn_3O_4 as compared to Mn_3O_4 nanoparticles. Fluorescence microscopy showed that almost 100% cells were viable when treated with phosphate buffered saline or Mn_3O_4 while only few dead cells were detected after exposure of HRG-Mn_3O_4 nanoparticles. However, laser irradiation resulted in massive cellular damage by HRG-Mn_3O_4 nanoparticles which was directly related to the generation of reactive oxygen species (ROS). **Conclusions**: HRG-Mn_3O_4 hybrid nanoparticles are stable, biocompatible, nontoxic, and possess therapeutic potential for photodynamic therapy of cancer. Further studies are warranted to explore the MRI imaging ability of these nanomaterials using animal models of cancer.

Keywords: hybrid nanoparticles; manganese oxide; graphene oxide; photodynamic therapy; cancer

1. Introduction

Tumor ablation is one of the minimally invasive techniques and is preferred for the treatment of tumors of the lung, kidney and liver. It provides an alternative for failed chemotherapy or radiotherapy or for non-surgical candidates. Ablation is also preferred as a first-line treatment in patients suffering from benign tumors of liver or small hepatocellular carcinoma [1]. Thermal ablation is performed by either heating or cooling of targeted tissues to cytotoxic level. Tumor cells are basically more vulnerable to heat as compared to normal cells because of differential sensitivity to hypoxia [2] and hydrogen ion concentration [3]. Interstitial laser ablation is yet another hyperthermic ablation procedure. The light generated by neodymium:yttrium aluminum garnet laser (1064 nm) is focused to the target tissue; the light is absorbed by the tissue and converted to heat for therapeutic purpose [1].

Photodynamic therapy (PDT) is a technique in which the cancer cells are exposed to light of specific wavelength after administration of nontoxic photosensitizers [4,5]. The excitation of photosensitizers by light exposure causes the emission of fluorescence as well as the generation of potentially toxic free radicals which impart photosensitizers the properties of both imaging and therapeutic agents [6–8]. One of the major disadvantages of PDT for combined imaging and treatment applications is the limited tissue penetration by visible light, for the activation of photosensitizers [9]. Therefore, there is a need to develop agents for PDT that can be activated by light at of 620–750 nm which is called as 'visible red optical window' [10]. At these wavelengths, body tissues are transparent, and the visible red radiation can be utilized to activate photosensitizers in deep tumors without causing any appreciable phototoxicity

to normal tissues. On the other hand chemotherapy is associated with systemic toxicity [11], whereas radiotherapy can damage adjacent normal tissue if an appropriate dose is not selected [12].

Graphene-based nanomaterials, in contrast to other types of carbon materials, possess a large surface area, are easy to functionalize and have improved solubility due to their unique optical, physicochemical and biomedical properties which enhance their applications in nanomedicine [13–15]. Graphene oxide (GO) nanoparticles functionalized with other materials have shown theranostic properties for cancer diagnosis and therapy [16,17]. Usman *et al.* [18] synthesized a GO-based delivery system for magnetic resonance imaging (MRI) using gadolinium nitrate as a contrast agent and naturally occurring protocatechuic acid as an anticancer compound. Yang *et al*. [19] have shown that manganese ferrite ($MnFe_2O_4$) nanoparticles deposited on GO show intense optical absorbance in the near infrared (NIR) region and high photothermal stability, which makes them highly efficient in photothermal ablation of cancer cells.

Manganese oxides, viz., MnO, MnO_2, Mn_2O_3, and Mn_3O_4, are attractive candidates for novel MRI contrast agent due to their inherent properties based on electronic configuration that can produce a large magnetic moment and cause nearby water protons relaxation [20]. Therefore, manganese oxides are one of the most widely investigated nanomaterials for image-guided therapeutic purposes [21,22]. In this study, we synthesized hybrid nanoparticles containing highly reduced graphene oxide and Mn_3O_4 (HRG-Mn_3O_4) and studied their biocompatibility as well as therapeutic potential for PDT of cancer, using a cellular model.

2. Materials and Methods

2.1 Chemicals and Reagents

All chemicals including solvents used for the synthesis of nanoparticles were procured from Sigma Aldrich (St. Louis, MO, USA). Graphite powder (99.999%) was obtained from Alfa Aesar, Kandel, Germany. Deionized water was prepared from a Millipore Milli-Q system and used in all experiments.

2.2 Preparation of Mn_3O_4 Nanoparticles

In a three-necked flask (100 mL capacity), a slurry of manganese (II) acetylacetonate was dissolved in oleylamine, keeping their molar ratio as 1:25, respectively. After heating the mixture at 162 °C for 11 h under nitrogen cover, the resultant mixture was allowed to cool to ambient temperature resulting in the formation of a brown suspension. The contents were centrifuged at 9000 rpm for 15 min, to collect a brown precipitate after removal of supernatant. Pure Mn_3O_4 was acquired after multiple washings of the brown precipitate with ethanol. The synthesized Mn_3O_4 has the tendency to be readily dispersed in typical organic solvents including dichloromethane, toluene and hexane. The synthesized Mn_3O_4 nanoparticles were vacuum dried before their usage.

2.3 Preparation of Highly Reduced Graphene Oxide (HRG)

Initially graphite oxide (GO) was synthesized from graphite powder and then using a modified Hummers method [23,24] and then it was converted to graphene oxide (GRO) following several steps of centrifugation, washing and finally sonication. GRO was reduced according to a previously reported method [25]. Briefly, GRO was dispersed in water and sonicated for 30 min. The resulting suspension was allowed to heat up to 100 °C and subsequently 3 mL of hydrazine hydrated were added. The temperature was slightly reduced (98 °C), and the suspension was kept under stirring for 24 h. Finally, a black powder was obtained which was filtered and washed several times with water. The resultant suspension was centrifuged at 4000 rpm for several 3 min, and the final product was collected via filtration and dried under vacuum.

2.4 Preparation of HRG-Mn_3O_4 Hybrid Nanoparticles

Approximately, 200 mg of Mn_3O_4 nanoparticles and 200 mg of highly reduced graphene powder were subjected to milling process using Fritsch Pulverisette P7 planetary ball mill (Idar-Oberstein, Germany) and stainless steel beads of 5 mm diameter. The nanocomposite powder and steel balls in the equal weight proportion (ratio 1:1) were introduced into the stainless steel container. The milling process of the components was allowed to continue for 16 h with intermittent pauses at regular intervals.

2.5 Characterization of Nanoparticles

The synthesized nanoparticles were characterized for size, elemental composition, physicochemical properties and stability using high resolution transmission electron microscopy (JEM-2100F, JEOL, Japan), energy-dispersive X-ray spectroscopy (EDX), UV–Vis spectroscopy (Perkin Elmer lambda 35, Waltham, MA, USA), FT-IR spectroscopy (Perkin Elmer 1000 FT-IR spectrometer), X-ray diffraction analysis (D2 Phaser X-ray diffractometer, Bruker, Germany) and thermogravimetric analysis (TGA/DSC1, Mettler Toledo AG, Analytical, Schwerzenbach, Switzerland).

2.6 Cytotoxicity Assay

The cytotoxicity of Mn_3O_4 and HRG-Mn_3O_4 nanoparticles was performed by 3-(4,5-dimethylthiazol-2-y1)-2,5-diphenyltetrazolium bromide (MTT) method. A549 cells were seeded in the 96-well plate (4×10^4 cells per well) in RPMI medium and incubated in the atmosphere of 5% CO_2 at 37 °C for 24 h. Different concentrations (6.25, 12.5, 25, 50 and 100 μg/mL) of Mn_3O_4 and HRG-Mn_3O_4 were added to the respective wells of micro plate followed by 4 h incubation. Phosphate

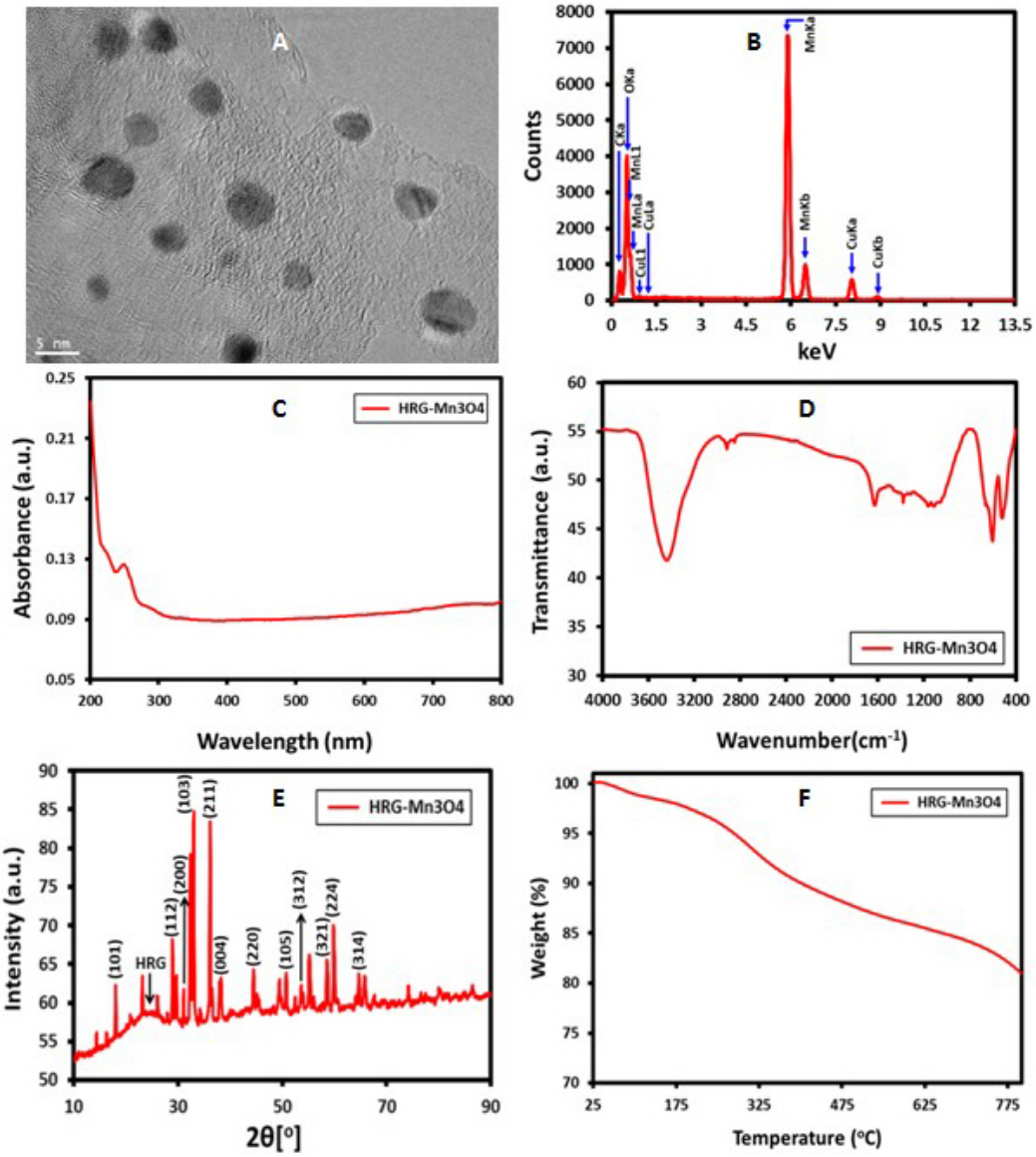

Fig. 1. Characterization of HRG-Mn_3O_4 nanoparticles using. (A) Transmission electron microscopy. (B) Energy-dispersive X-ray spectroscopy. (C) UV-visible spectroscopy. (D) FT-IR. (E) X-ray diffraction analysis. (F) Thermogravimetric analysis.

buffer saline (PBS) and triton X-100 were used as control and negative control, respectively. For laser-induced phototoxicity analysis, the cells were treated with a 670 nm laser irradiation at 0.1 W/cm^2 for 5 min and further incubated for 24 h. Aqueous solution of MTT (50 μL) was added to the wells of micro plate, 4 h before the termination of incubation period (24 h). After discarding the upper layer, MTT solubilization solution, DMSO (100 μL) was added to all the wells of the micro plate for dissolving the formazan crystals followed by measuring the absorbance at 590 nm, which was converted to cell viability based on absorbance of dissolved formazan. The percent cell viability was calculated using the following equation:

$$\text{Percent cell viability} = (\text{sample cells absorbance}/\text{control cells absorbance}) \times 100$$

2.7 Fluorescence Microscopy of Live and Dead Cells

The live/dead assay kit containing fluorescein diacetate (FDA) and propidium iodide (PI) to visualize live and dead cells, respectively was used and cells were visualized under fluorescence microscope. A549 cells (2×10^4 cells per well) were seeded on a 24 well plate and incubated in the atmosphere of 5% CO_2 at 37 °C for 24 h. Mn_3O_4 and HRG-Mn_3O_4 nanoparticles (50 μg/mL) were added to the 24 well plate. PBS was used as a control and the plate was incubated for 4 h. Then cells were exposed to a 670 nm laser irradiation at 0.1 W/cm^2 for 5 min and further incu-

bated for 24 h. FDA and PI were added to treated cells and incubated for 5 min. Then the cells were washed with PBS thrice to remove excess FDA/PI and fluorescence images were acquired by a fluorescence microscope with 490 nm excitation and emission at 525 nm.

2.8 Detection of Intracellular Reactive Oxygen Species (ROS)

For intracellular ROS detection, A549 cells (2×10^4 cells per well) were incubated in 24-well plate with 5% CO_2 at 37 °C for 12 h. HRG–Mn_3O_4 nanoparticles diluted in media to yield a final concentration of 50 μg/mL, were added to the cells and incubated for 4 h. The incubated cells were irradiated with 670 nm laser (0.1 W/cm^2) for 5 min and cells were washed with PBS. Serum free medium containing 2,7-dichlorodihydrofluorescein diacetate (DCFH-DA) (20 μM) was added into the wells and the plate was incubated for another 15 min. Then the cells were washed with PBS thrice to remove excess DCFH-DA and fluorescence images were acquired by fluorescence microscope with 485 nm excitation and emission at 530 nm wavelengths. DCFH-DA has been used extensively for total ROS detection. After cellular uptake, DCFH-DA is cleaved off the acetyl groups by cellular esterase, resulting in the formation of DCFH, which is oxidized by ROS to produce 2,7-dichlorofluorescein (DCF), which emits green fluorescence at excitation and emission wavelengths of 485 nm and 530 nm, respectively [26].

2.9 Statistics

All the cell based analyses were performed in triplicate and the results reported as means $\pm$ standard deviation. The data were analyzed by one-way analysis of variance (ANOVA) followed by Dunnett's test. p values < 0.05 were considered as statistically significant.

3. Results

3.1 Characterization of Nanoparticles

The shape of hybrid nanoparticles appeared as round with the average diameter of 12 $\pm$ 2.21 nm (Fig. 1A). In EDX analysis, the intense signals at 0.65, 5.88, and 6.62 keV strongly suggests that 'Mn' was the major element, which has an optical absorption in this range owing to the surface plasmon resonance (SPR). The other signals found in the range 0.0–0.5 keV signify the absorption of carbon and oxygen, confirming the formation of HRG-Mn_3O_4 nanocomposite (Fig. 1B). UV-Vis spectrum of HRG-Mn_3O_4 nanoparticles showed respective absorption bands at ~220 (Mn_3O_4) and ~270 nm (HRG) indicating the formation of HRG-Mn_3O_4 (Fig. 1C). FT-IR spectrum of HRG-Mn_3O_4 displayed the graphene oxide bands at ~1630 cm^{-1} (for C=C stretching), ~1209 cm^{-1} (for C–O–C stretching), ~1050 cm^{-1} (for C–O stretching), and a broad band at around 3440 cm^{-1} for hydroxyl groups indicated the presence of various oxygen-containing functional groups, such as carbonyl, carboxylic, epoxy, and hydroxyl groups in graphene oxide. The removal of oxygen-containing groups of graphene oxide in HRG was indicated by the disappearance of some of the bands such as the band at ~1740 (which is present in HRG only; spectrum not shown). Also the relative decrease in the intensity of some of the bands, like the decrease in intensity of broad band at 3440 cm^{-1} points towards the reduction of graphene oxide. The existence of other absorption bands of Mn at 624 and 525 cm^{-1} clearly indicated the formation of HRG-Mn_3O_4 nanocomposite (Fig. 1D). The XRD patterns of Mn_3O_4 nanoparticles such as 18.2° (101), 29.1° (112), 31.2° (200), 32.5° (103), 36.3° (211), 38.2° (004), 44.6° (220), 50.8° (105), 53.8° (312), 58.7° (321), 60.0° (224), and 64.8° (314) indicated the formation of manganese oxide. XRD pattern of HRG-Mn_3O_4 with the appearance of a broad peak at ~22.4° (002) confirmed the reduction of graphene oxide in the form of HRG. The existence of all these reflections indicates the formation of HRG-Mn_3O_4 nanoparticles (Fig. 1E). TGA analysis of HRG-Mn_3O_4 nanoparticles displays the weight loss of about 20% after heating up to 800 °C indicating the presence of substantial oxygen functionalities despite appreciable stability of hybrid nanoparticles at high temperatures (Fig. 1F).

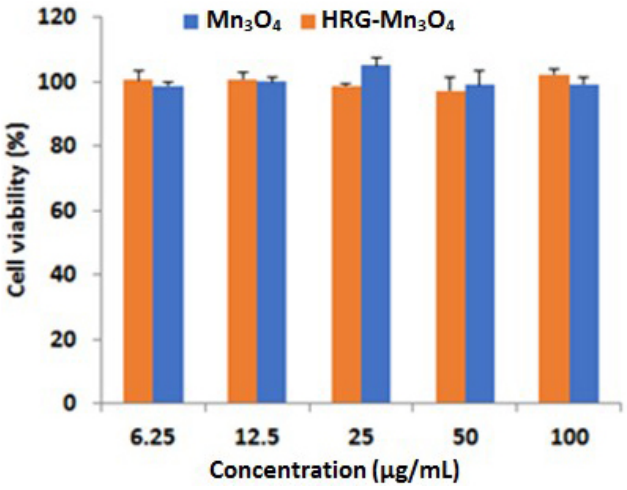

Fig. 2. Cytotoxicity analysis showing cell viability of A549 cells treated with different concentrations of Mn_3O_4 and HRG-Mn_3O_4 nanoparticles.

3.2 Cytotoxicity and In-Vitro PDT

The cytotoxicity analysis using MTT assay showed that more than 98% of A549 cells survived even after the exposure of a high concentration (100 μg/mL) of nanomaterials indicating the biocompatibility of both Mn_3O_4 and HRG-Mn_3O_4 nanoparticles (Fig. 2). Almost 100% cells were viable when treated with phosphate buffered saline (PBS) or Mn_3O_4 nanoparticles in presence of 670 nm laser irradiation (0.1 W/cm^2) for 5 min (Fig. 3). However,

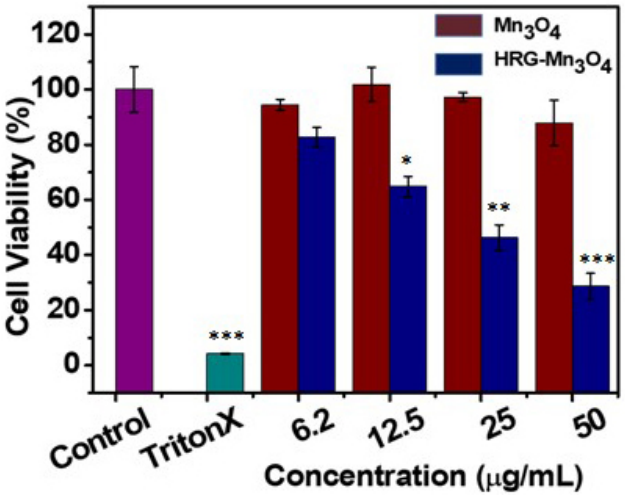

Fig. 3. Cell viability of A549 cells incubated with different concentrations of PBS (control), Triton X100 (negative control), Mn_3O_4 and HRG-Mn_3O_4 nanoparticles in presence of 670 nm laser irradiation (0.1 W/cm^2) for 5 min. Data are represented as mean ± standard deviation (n = 3). * $p < 0.05$, ** $p < 0.01$ and *** $p < 0.001$ versus respective control groups.

laser irradiation resulted in significant and concentration-dependent cellular damage by HRG-Mn_3O_4 nanoparticles (Fig. 3).

3.3 Live/Dead Cell Analysis

To study the interactions between cells and the nanoparticles, we used the visible red optical imaging of A549 cells after incubation in PBS, Mn_3O_4 nanoparticles, HRG-Mn_3O_4 nanoparticles and HRG-Mn_3O_4 nanoparticles with and without laser irradiation for 5 min (Fig. 4). After 5 min, propidium iodide (PI) (red emission for dead cells) fluorescent dots were observed in HRG-Mn_3O_4 nanoparticles plus laser treated group when compared to HRG-Mn_3O_4 nanoparticles treated cells. However, no red fluorescent dots were observed in PBS and Mn_3O_4 treated A549 groups of cells. On the other hand, A549 cells incubated in PBS, Mn_3O_4 nanoparticles, HRG-Mn_3O_4 nanoparticles showed abundant green emission indicating the presence of live cells (Fig. 4).

3.4 Intracellular ROS Generation

The intracellular ROS production was investigated by fluorescence microscopy with cell permeable green fluorescence ROS indicator DCFH-DA. As shown in Fig. 5D, HRG-Mn_3O_4 nanoparticles increased the intracellular ROS generation in A549 cells in presence of laser irradiation. A remarkable green fluorescence of DCF was observed with HRG-Mn_3O_4 in presence of laser irradiation whereas the green fluorescence is negligible for control cells (Fig. 5A).

4. Discussion

In this study, we synthesized hybrid nanoparticles containing the equal amounts of two moieties, highly reduced graphene (HRG) and Mn_3O_4. Both these constituents have specific properties; HRG is effective for optical imaging and PDT whereas Mn_3O_4 possesses MRI imaging property. Manganese oxide nanoparticles have been shown to be a promising $\mathbf{T}_1$-weighted contrast agent with high magnetization spins and fast water proton exchange rates [27]. Therefore, manganese oxide nanoparticles are emerging as potentially useful MRI contrast agents for biomedical imaging and tumor diagnosis [28]. Although, manganese oxide nanoparticles with good crystallinity can easily be synthesized on a large scale under mild and ambient reaction conditions, it is difficult to design and synthesize highly stable Mn^{2+} complexes with high sensitivities for clinical applications [29]. This drawback can be overcome by building manganese-based nanoparticulate systems, such as MnO, Mn_3O_4, Mn_3O_4-SiO_2 [30]. Combination of optical and MRI imaging has emerged as an attractive technique for both *in-vivo* animal and clinical cancer diagnosis [31]. In recent years, there is a trend of theranostic nanoparticles possessing the capability of imaging and therapy together [8,13,32].

We performed *in-vitro* cytotoxicity assay to investigate the toxicity profile of newly synthesized HRG-Mn_3O_4 hybrid nanoparticles. *In-vitro* cytotoxicity studies of nanoparticles are preferred as they are simple, cost-effective and faster than *in-vivo* models [33]. These results confirmed that the HRG-Mn_3O_4 nanoparticles are nontoxic and biocompatible under physiological conditions (Fig. 2). The commonly used contrasting agents which are based on gadolinium (Gd) cause kidney fibrosis in some cases necessitating the search for alternative agents. Xiao *et al.* [34] synthesized Mn_3O_4 nanoparticles that showed high relaxivity, twice higher than that of commercially used contrasting agents [35]. Mn_3O_4 NPs coated with polyethylene glycol (PEG), designed as MRI contrasting agent, have shown good biocompatibility after intravenous injection in mice [20]. Previous studies have shown that graphene oxide nanoparticles are less toxic to different cell lines with a survival rate exceeding 80% at a high concentration of 200 μg/mL [36,37]. Wang *et al.* [38] observed that graphene oxide is nontoxic at low and medium doses whereas high doses cause significant toxicity, both *in-vitro* and *in-vivo*, with a strong tendency to affect lung, liver, spleen and kidney.

The cell viability analysis of newly synthesized nanoparticles was investigated in A549 cells treated with Mn_3O_4 or hybrid HRG-Mn_3O_4 nanoparticles. After laser irradiation, a significant and concentration-dependent cytotoxicity of HRG-Mn_3O_4 was observed as compared to Mn_3O_4 nanoparticles (Fig. 3). These findings were confirmed by fluorescence microscopy imaging of live/dead cells after exposure to various treatments (Fig. 4). We ob-

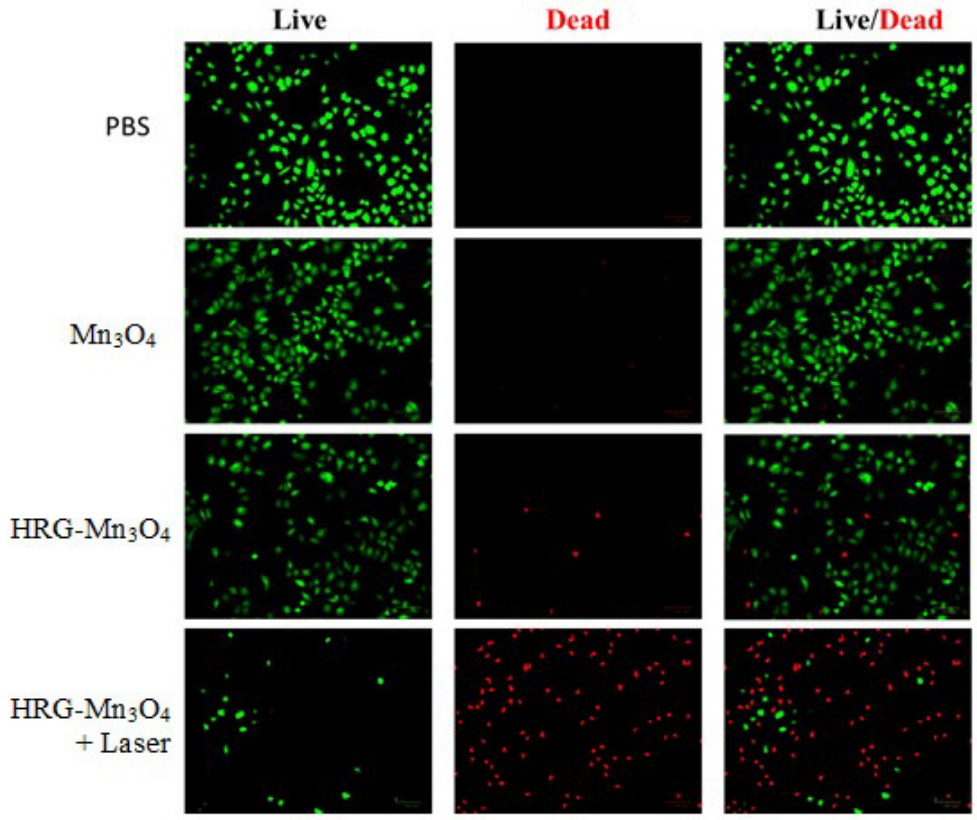

Fig. 4. Fluorescence microscopy images of A549 cells co-stained with fluorescein diacetate (green emission for live cells) and propidium iodide (red emission for dead cells) with PBS (control), HRG-Mn_3O_4 nanoparticles with/without laser irradiation (670 nm, 0.1 W/cm^2) for 5 min.

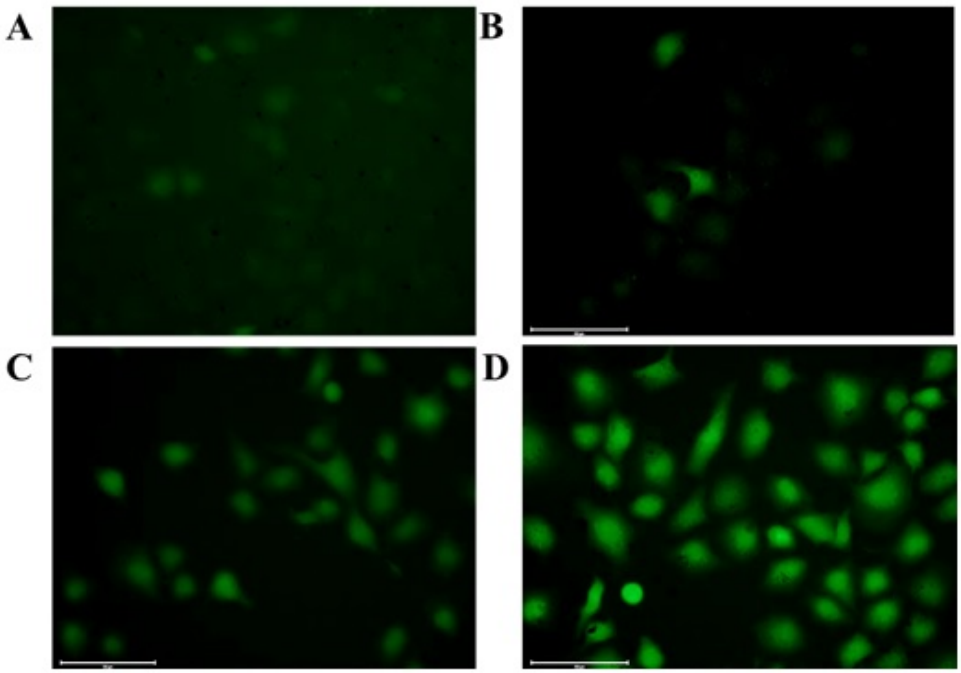

Fig. 5. Fluorescence microscopy images of A549 cells under different treatments. (A) Incubated with only DCFH-DA. (B) Incubated with DCFH-DA + Mn_3O_4. (C) Incubated with DCFH-DA + HRG-Mn_3O_4. (D) Incubated with DCFH-DA + HRG-Mn_3O_4+ laser irradiation (670 nm, 0.1 W/cm^2) for 5 min (scale bar: 100 μm).

served that hybrid nanoparticles produced cytotoxicity only after laser irradiation suggesting their potential for PDT of cancer. The results of DCFH-DA fluorescence microscopy showed excessive generation of ROS in A549 cells exposed to HRG-Mn_3O_4 nanoparticles and laser irradiation (Fig. 5). Because of the limited migration of $^1O_2$ from its formation site [39], the location of cellular and tissue damage by PDT are mainly related to the localization of the photosensitizer [40]. Those photosensitizers which are not taken up by cells have been found to be extremely inefficient even their ability of producing high yield of $^1O_2$ [41]. Moreover, since most PDT sensitizers do not accumulate in cell nuclei, PDT has generally a low potential of causing DNA damage, mutations, and carcinogenesis [42]. Photosensitizers that preferentially localize in mitochondria usually induce apoptosis whereas the photosensitizers that localized in plasma membrane tend to cause necrosis during the exposure of light [41]. Another important parameter that can affect cytotoxicity is the availability of oxygen within the tissue receiving PDT treatment. The rates of $^1O_2$ generation and hence tissue oxygen consumption are high when both photosensitizer level and the exposure of light are high [43,44].

Graphene based materials are excellent photosensitizers [45] and showed improved anticancer PDT effects compared to the conventional photosensitizers [46]. The photoactivation of a photosensitizer initially enables its excitation to a triplet state through a transient intermediate called 'singlet state'. The electron and energy transfer to surrounding free oxygen produces potentially toxic reactive oxygen species (ROS), including superoxide anion radical, hydroxyl radical, and hydrogen peroxide. Excessive generation of toxic ROS causes tumor cell death by oxidative stress, as schematically presented in Fig. 6. Although, GO in a low concentration (10 μg/mL) did not enter A549 cells and had no obvious toxicity, the higher concentration of GO (200 μg/mL) caused oxidative stress and induced a slight loss of cell viability [37]. Enhancement of killing of cancer cells exposed to HRG-Mn_3O_4 nanoparticles followed by laser irradiation is associated with enhanced generation of ROS resulting in lipid peroxidation and disruption of cellular membranes causing cell death [16].

5. Conclusions

The newly synthesized HRG-Mn_3O_4 hybrid nanoparticles do not pose any cytotoxicity at normal physiological conditions and therefore they are biocompatible. However, exposure of laser light of specific wavelength resulted in massive cellular damage by HRG-Mn_3O_4 nanoparticles, which was directly related to generation of intracellular ROS. These findings suggest a great potential of HRG-Mn_3O_4 nanoparticles for photodynamic therapy. Further studies are warranted to explore their MRI imaging property and *in-vivo* anticancer activity using animal models of cancer.

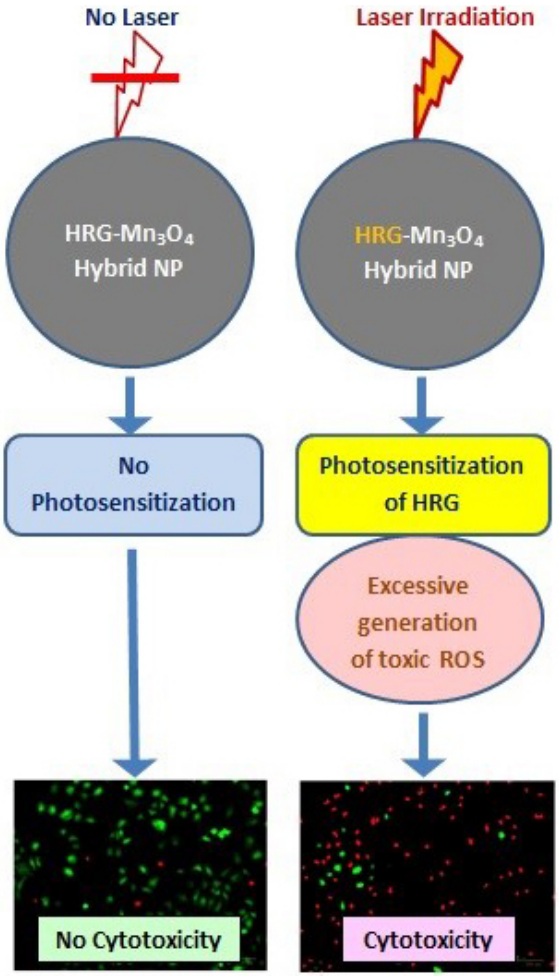

Fig. 6. Schematic presentation of mechanism of HRG-Mn_3O_4 induced cytotoxicity under laser irradiation.

6. Limitations

In this study, we compared HRG-Mn_3O_4 hybrid nanoparticles with Mn_3O_4 nanoparticles whereas the PDT potential of HRG alone was not evaluated. Although, it is the HRG moiety in HRG-Mn_3O_4 hybrid nanoparticles that is mainly responsible for killing the cancer cells under laser irradiation however it is important to find out whether the presence of Mn_3O_4 in HRG-Mn_3O_4 hybrid nanoparticles affects the PDT potential of HRG or not, by testing the effect of HRG alone. Another limitation of this study is the use of only one type of cancer cells (A549); use of more than one cell line would certainly result in broader implications.

Availability of Data and Materials

Data contained within the article.

Author Contributions

Conceptualization—HAK; Methodology—HAK, YKL, MRSha, ASA; Formal analysis—MRSha, STA, AAE, ASA; Investigation—HAK, YKL, MRSid;

Resources—HAK, YKL; Data curation—HAK, YKL, MRSid, AAE; Original draft preparation—HAK, NJS, YKL, MRSha; Writing, review and editing—HAK, NJS, MRSha; Supervision—HAK; Project administration—HAK, STA; Funding acquisition—HAK.

Ethics Approval and Consent to Participate

The study protocol was approved by Institutional Review Board (Approval No. KSU-SE-21-23).

Acknowledgment

We acknowledge excellent technical support from laboratory staff.

Funding

National Plan for Science, Technology and Innovation (MAARIFAH), King Abdulaziz City for Science and Technology, Kingdom of Saudi Arabia, Award Number (14-NAN-862-02).

Conflict of Interest

Given his role as Guest Editor and member of Editorial Board, Haseeb Khan had no involvement in the peer-review of this article and has no access to information regarding its peer-review. Full responsibility for the editorial process for this article was delegated to Peter Brenneisen.

References

[1] Knavel EM, Brace CL. Tumor ablation: common modalities and general practices. Techniques in Vascular and Interventional Radiology. 2013; 16: 192–200.

[2] Nikfarjam M, Muralidharan V, Christophi C. Mechanisms of focal heat destruction of liver tumors. The Journal of Surgical Research. 2005; 127: 208–223.

[3] Overgaard J. Influence of extracellular pH on the viability and morphology of tumor cells exposed to hyperthermia. Journal of the National Cancer Institute. 1976; 56: 1243–1250.

[4] Gage AA, Baust J. Mechanisms of tissue injury in cryosurgery. Cryobiology. 1998; 37: 171–186.

[5] Lee EW, Thai S, Kee ST. Irreversible electroporation: a novel image-guided cancer therapy. Gut and Liver. 2010; 4: S99–S104.

[6] Davalos RV, Mir ILM, Rubinsky B. Tissue ablation with irreversible electroporation. Annals of Biomedical Engineering. 2005; 33: 223–231.

[7] Ahmed M, Brace CL, Lee FT, Goldberg SN. Principles of and advances in percutaneous ablation. Radiology. 2011; 258: 351–369.

[8] Kang SH, Nafiujjaman M, Nurunnabi M, Li L, Khan HA, Cho KJ, *et al*. Hybrid photoactive nanomaterial composed of gold nanoparticles, pheophorbide-A and hyaluronic acid as a targeted bimodal phototherapy. Macromolecular Research. 2015; 23: 474-484.

[9] Mac Donald IJ, Dougherty TJ. Basic principles of photodynamic therapy. Journal of Porphyrins and Phthalocyanines. 2001; 5: 105–129.

[10] Sekkat N, van den Bergh H, Nyokong T, Lange N. Like a bolt from the blue: phthalocyanines in biomedical optics. Molecules. 2011; 17: 98–144.

[11] Plenderleith IH. Treating the treatment: toxicity of cancer chemotherapy. Canadian Family Physician Medecin De Famille Canadien. 1990; 36: 1827–1830.

[12] Khan HA. CalcNTCP: a simple tool for computation of normal tissue complication probability (NTCP) associated with cancer radiotherapy. International Journal of Radiation Biology. 2007; 83: 717–720.

[13] Lage T, Rodrigues RO, Catarino S, Gallo J, Bañobre-López M, Minas G. Graphene-Based Magnetic Nanoparticles for Theranostics: An Overview for Their Potential in Clinical Application. Nanomaterials. 2021; 11: 1073.

[14] Nurunnabi M, Parvez K, Nafiujjaman M, Revuri V, Khan HA, Feng X, *et al*. Bioapplication of graphene oxide derivatives: drug/gene delivery, imaging, polymeric modification, toxicology, therapeutics and challenges. RSC Advances. 2015; 5: 42141–42161.

[15] Goenka S, Sant V, Sant S. Graphene-based nanomaterials for drug delivery and tissue engineering. Journal of Controlled Release. 2014; 173: 75–88.

[16] Nafiujjaman M, Nurunnabi M, Kang S, Reeck GR, Khan HA, Lee Y. Ternary graphene quantum dot-polydopamine-Mn_3O_4 nanoparticles for optical imaging guided photodynamic therapy and T_1-weighted magnetic resonance imaging. Journal of Materials Chemistry B. 2015; 3: 5815–5823.

[17] Nafiujjaman M, Khan HA, Lee Y. Peptide-influenced graphene quantum dots on iron oxide nanoparticles for dual imaging of lung cancer cells. Journal of Nanoscience and Nanotechnology. 2017; 17: 1704–1711.

[18] Usman MS, Hussein MZ, Kura AU, Fakurazi S, Masarudin MJ, Ahmad Saad FF. Graphene Oxide as a Nanocarrier for a Theranostics Delivery System of Protocatechuic Acid and Gadolinium/Gold Nanoparticles. Molecules. 2018; 23: 500.

[19] Yang Y, Shi H, Wang Y, Shi B, Guo L, Wu D, *et al*. Graphene oxide/manganese ferrite nanohybrids for magnetic resonance imaging, photothermal therapy and drug delivery. Journal of Biomaterials Applications. 2016; 30: 810–822.

[20] Cai X, Zhu Q, Zeng Y, Zeng Q, Chen X, Zhan Y. Manganese Oxide Nanoparticles As MRI Contrast Agents In Tumor Multimodal Imaging And Therapy. International Journal of Nanomedicine. 2019; 14: 8321–8344.

[21] Zhan Y, Zhan W, Li H, Xu X, Cao X, Zhu S, *et al*. In Vivo Dual-Modality Fluorescence and Magnetic Resonance Imaging-Guided Lymph Node Mapping with Good Biocompatibility Manganese Oxide Nanoparticles. Molecules. 2017; 22: 2208.

[22] Zhen Z, Xie J. Development of manganese-based nanoparticles as contrast probes for magnetic resonance imaging. Theranostics. 2012; 2: 45–54.

[23] Hummers WS, Offeman RE. Preparation of graphitic oxide. Journal of the American Chemical Society. 1958; 80: 1339.

[24] Alam SN, Sharma N, Kumar L. Synthesis of graphene oxide (GO) by modified Hummers method and its thermal reduction to obtain reduced graphene oxide (rGO). Graphenes. 2017; 6: 1–18.

[25] Assal ME, Shaik MR, Kuniyil M, Khan M, Alzahrani AY, Al-Warthan A, *et al*. Mixed zinc/manganese on highly reduced graphene oxide: A highly active nanocomposite catalyst for aerial oxidation of benzylic alcohols. Catalysts. 2017; 7: 391.

[26] Kim H, Xue X. Detection of total reactive oxygen species in adherent cells by 2',7'-Dichlorodihydrofluorescein diacetate staining. Journal of Visualized Experiments. 2020; 160: e60682.

[27] Na HB, Song IC, Hyeon T. Inorganic nanoparticles for MRI contrast agents. Advanced Materials. 2009; 21: 2133–2148.

[28] Shin J, Anisur RM, Ko MK, Im GH, Lee JH, Lee IS. Hollow manganese oxide nanoparticles as multifunctional agents for magnetic resonance imaging and drug delivery. Angewandte Chemie. 2009; 48: 321–324.

[29] Yu T, Moon J, Park J, Park YI, Na HB, Kim BH, *et al*. Various-shaped uniform Mn3O4 nanocrystals synthesized at low temperature in air Atmosphere. Chemistry of Materials. 2009; 21: 2272–2279.
[30] Zhu D, Liu F, Ma L, Liu D, Wang Z. Nanoparticle-based systems for T(1)-weighted magnetic resonance imaging contrast agents. International Journal of Molecular Sciences. 2013; 14: 10591–10607.
[31] Zhan Y, Shi S, Ehlerding EB, Graves SA, Goel S, Engle JW, *et al*. Radiolabeled, Antibody-Conjugated Manganese Oxide Nanoparticles for Tumor Vasculature Targeted Positron Emission Tomography and Magnetic Resonance Imaging. ACS Applied Materials & Interfaces. 2017; 9: 38304–38312.
[32] Khatun Z, Nurunnabi M, Nafiujjaman M, Reeck G, Khan HA, Cho KJ, *et al*. A hyaluronic acid nanogel for photo-chemo theranostic of lung cancer with simultaneous light-responsive controlled release of doxorubicin. Nanoscale. 2015; 7: 10680–10689.
[33] Fischer HC, Chan WCW. Nanotoxicity: the growing need for in vivo study. Current Opinion in Biotechnology. 2007; 18: 565–571.
[34] Xiao J, Tian XM, Yang C, Liu P, Luo NQ, Liang Y, *et al*. Ultrahigh relaxivity and safe probes of manganese oxide nanoparticles for in vivo imaging. Scientific Reports. 2013; 3: 3424.
[35] Sobańska Z, Roszak J, Kowalczyk K, Stępnik M. Applications and Biological Activity of Nanoparticles of Manganese and Manganese Oxides in In Vitro and In Vivo Models. Nanomaterials. 2021; 11: 1084.
[36] Liao K, Lin Y, Macosko CW, Haynes CL. Cytotoxicity of graphene oxide and graphene in human erythrocytes and skin fibroblasts. ACS Applied Materials & Interfaces. 2011; 3: 2607–2615.
[37] Chang Y, Yang S, Liu J, Dong E, Wang Y, Cao A, *et al*. In vitro toxicity evaluation of graphene oxide on A549 cells. Toxicology Letters. 2011; 200: 201–210.
[38] Wang K, Ruan J, Song H, Zhang J, Wo Y, Guo S, *et al*. Biocompatibility of Graphene Oxide. Nanoscale Research Letters. 2011; 6: 8.
[39] Moan J, Berg K. The photodegradation of porphyrins in cells can be used to estimate the lifetime of singlet oxygen. Photochemistry and Photobiology. 1991; 53: 549–553.
[40] Peng Q, Moan J, Nesland JM. Correlation of subcellular and intratumoral photosensitizer localization with ultrastructural features after photodynamic therapy. Ultrastructural Pathology. 1996; 20: 109–129.
[41] Dougherty TJ, Gomer CJ, Henderson BW, Jori G, Kessel D, Korbelik M, *et al*. Photodynamic therapy. Journal of the National Cancer Institute. 1998; 90: 889–905.
[42] Moan J. Porphyrin photosensitization and phototherapy. Photochemistry and Photobiology. 1986; 43: 681–690.
[43] Nichols MG, Foster TH. Oxygen diffusion and reaction kinetics in the photodynamic therapy of multicell tumour spheroids. Physics in Medicine and Biology. 1994; 39: 2161–2181.
[44] Zilberstein J, Bromberg A, Frantz A, Rosenbach-Belkin V, Kritzmann A, Pfefermann R, *et al*. Light-dependent oxygen consumption in bacteriochlorophyll-serine-treated melanoma tumors: on-line determination using a tissue-inserted oxygen microsensor. Photochemistry and Photobiology. 1997; 65: 1012–1019.
[45] Chen D, Dougherty CA, Zhu K, Hong H. Theranostic applications of carbon nanomaterials in cancer: Focus on imaging and cargo delivery. Journal of Controlled Release. 2015; 210: 230–245.
[46] Hu Z, Li J, Huang Y, Chen L, Li Z. Functionalized graphene/C 60 nanohybrid for targeting photothermally enhanced photodynamic therapy. RSC Advances. 2015; 5: 654–664.